# High-Performance Hybrid Phenyl-C61-Butyric Acid Methyl Ester/Cd₃P₂ Nanowire Ultraviolet−Visible−Near Infrared Photodetectors

Gui Chen,[†,‡] Bo Liang,[†,‡] Xi Liu,[§] Zhe Liu,[†,‡] Gang Yu,[‡] Xuming Xie,[†,‡] Tao Luo,[†,‡] Di Chen,[‡] Mingqiang Zhu,[‡,*] Guozhen Shen,[†,*] and Zhiyong Fan[§,*]

[†]State Key Laboratory for Superlattices and Microstructures, Institute of Semiconductors, Chinese Academy of Sciences, Beijing 100083, China, [‡]Wuhan National Laboratory for Optoelectronics (WNLO) and School of Optical and Electronic Information, Huazhong University of Science and Technology (HUST), Wuhan 430074, China, and [§]Department of Electronic and Computer Engineering, Hong Kong University of Science and Technology, Clear Water Bay, Kowloon, Hong Kong, China

ABSTRACT In this work, single-crystalline p-type Cd_3P_2 nanowires (NWs) were synthesized on a Cd sheet *via* a facile chemical vapor deposition method. Then field-effect transistors and high-performance photodetectors were fabricated based on these NWs. It was found that hole mobility of a pristine Cd_3P_2 NW is around 2.94 cm^2 V^{-1} s^{-1}. Meanwhile, high responsivity and photoconductive gain were observed on these devices across a broad spectral range covering UV−visible to NIR with high stability and reproducibility. Furthermore, hybrid organic−inorganic n-type phenyl-C61-butyric acid methyl ester (PCBM) and p-type Cd_3P_2 NW heterojunction photodetectors were also fabricated, exhibiting much improved photocurrent and photoconductive gain, as compared to the device made of pristine Cd_3P_2 NWs. Intriguingly, the flexible hybrid photodetectors have been fabricated on plastic substrates and characterized under various bending conditions, demonstrating their excellent flexibility and robustness. The high performance and flexibility of the hybrid photodetectors are promising for further applications requiring large-area, high-sensitivity, and high-speed photodetectors with broad-spectrum photoresponse.
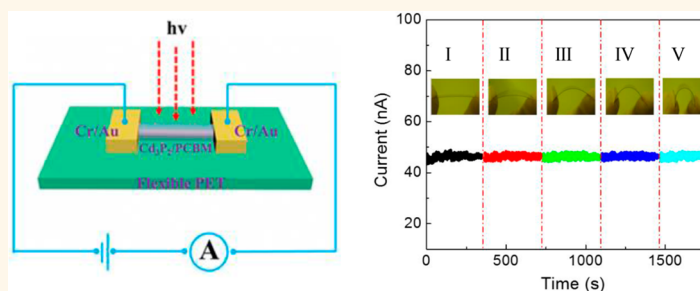
KEYWORDS: Cd_3P_2 NWs · organic−inorganic hybrid device · UV−visible−NIR · flexible photodetector

One-dimensional (1D) semiconducting NWs have attracted much attention in the past decades due to their high aspect ratio, large surface-to-volume ratio, and surface with dangling bonds that can be modified and functionalized. These properties triggered enormous interest to utilize them as building blocks for novel nanoscale devices, *e.g.* field-effect transistors (FETs), chemical/biosensors, lithium-ion batteries, solar cells, and photodetectors.[1−21] Recently, 1D semiconducting NW-based FET photodetectors have been proved highly responsive to broadband light from ultraviolet−visible to near-infrared,[22−24] which makes them potentially applicable for optical communication, optical interconnects, and high-resolution image sensing techniques.[25−28] Typically, narrow band gap

materials are responsive to broad-spectrum light. In fact, cadmium phosphide (Cd_3P_2), as an important II−V group compound semiconductor, has a small band gap of 0.55 eV, thus is a potential material that can respond to light with wavelengths up to 2.2 μm. Despite the extensive research on the growth and optical properties of Cd_3P_2 nanostructures with different morphologies,[29−36] studies on Cd_3P_2 NWs synthesis and its applications in electronic and optoelectronic devices, especially UV−visible−NIR photodetectors, have rarely been reported.

In this work, synthesis of single-crystalline Cd_3P_2 NWs on Cd foil *via* a facile chemical vapor deposition (CVD) method is reported. High-performance p-type single Cd_3P_2 NW devices were fabricated as photodetectors
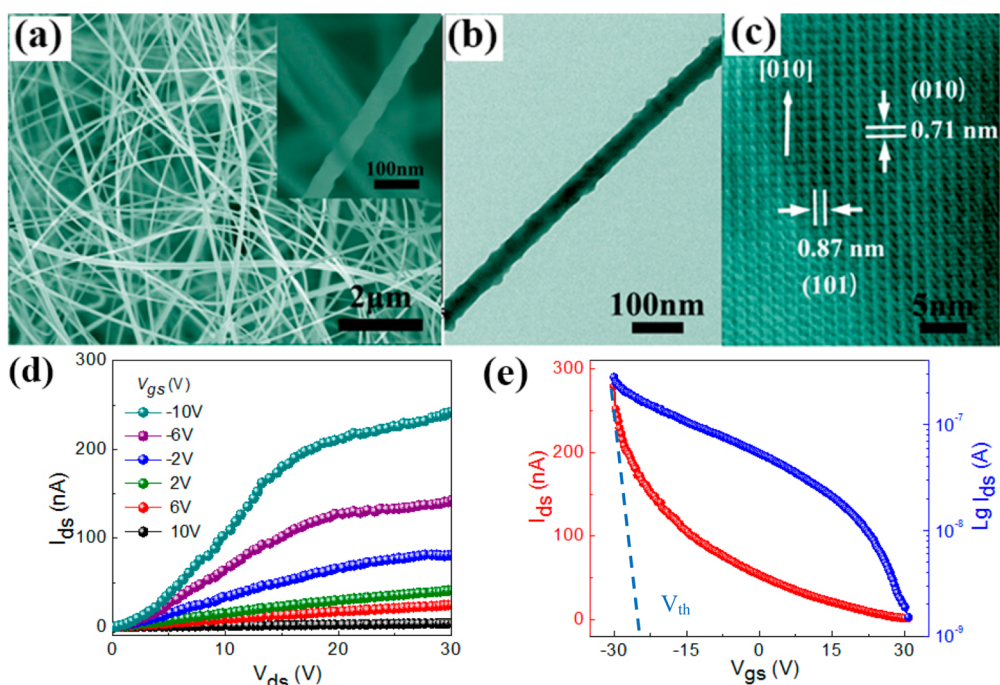
Figure 1. (a) SEM image, (b) TEM image, and (c) HRTEM images of as-synthesized Cd_3P_2 NWs. Inset shows a single Cd_3P_2 NW. (d) I_{ds} versus V_{ds} curves measured at room temperature with gate voltages from −10 to 10 V at a step of 4 V. (e) Corresponding I_{ds} versus V_{gs} curves of the device at V_{ds} = 10 V.

for the first time, followed by systematic investigation of their optoelectronic properties. Furthermore, by utilizing n-type phenyl-C61-butyric acid methyl ester (PCBM) and p-type Cd_3P_2 NWs as the components, the hybrid PCBM:single Cd_3P_2 NW photodetectors were successfully fabricated on a rigid SiO_2/Si substrate and a flexible PET substrate, respectively, demonstrating largely improved photocurrent and photoconductive gain. These results indicate that the hybrid PCBM:Cd_3P_2 NW photodetectors are highly promising candidates for further applications requiring large-area, high-sensitivity, and high-speed photodetectors with broad-spectrum photoresponse.

RESULTS AND DISCUSSION

Synthesis and Structural Analysis. Figure 1a shows the typical scanning electron microscopy (SEM) image of the as-grown Cd_3P_2 NWs. The Cd foil was found densely covered with a large number of Cd_3P_2 NWs with lengths of several tens to hundreds of micrometers and diameters in the range 50−250 nm. The composition of the Cd_3P_2 NWs was detected by energy-dispersive spectrum (EDS) measurements, and the corresponding spectrum is shown in Figure S1. It suggests that the NW is composed of Cd and P elements with an atomic ratio close to 3:2, and no other impurity elements are identified within the detection limit of EDS, which evidences the formation of pure Cd_3P_2 product. Figure 1b shows the transmission electron microscopy (TEM) image of a single Cd_3P_2 NW with a diameter of 50 nm. The

high-resolution TEM (HRTEM) image taken from the Cd_3P_2 NW in Figure 1b is shown in Figure 1c, which demonstrates its single-crystalline nature. The two sets of lattice fringes along and perpendicular to the longitudinal axis of the NW are 0.87 and 0.71 nm, respectively, corresponding to the (010) and (101) planes of tetragonal structure of Cd_3P_2,[34] indicating the growth direction is parallel to the (010) plane.

Electronic Transport and Photoresponse Properties of a Single Cd_3P_2 NW. In order to study the electronic transport properties of the Cd_3P_2 NWs, FETs based on a single Cd_3P_2 NW were fabricated on 500 nm SiO_2 coated Si substrate. Figure 1d displays the source−drain current (I_{ds}) versus source−drain voltage (V_{ds}) curves measured at different gate voltages (V_{gs}) from −10 V to +10 V. From these curves, it can be seen that the conductance of the device progressively decreases with increased V_{gs}, revealing the typical p-type semiconductor behavior. The source−drain currents (I_{ds}) versus gate voltage (V_{gs}) curve at a given V_{ds} = 10 V was also measured, and the result is depicted in Figure 1e, which also shows decreased I_{ds} when increasing V_{gs}, with a clear turning off at around −24 V (V_T = −24 V). In fact, the on−off ratio was found to be about ∼10^2. Meanwhile, the transconductance (g_m) can be deduced from the linear regime of the I_{ds}−V_{gs} curve via the equation
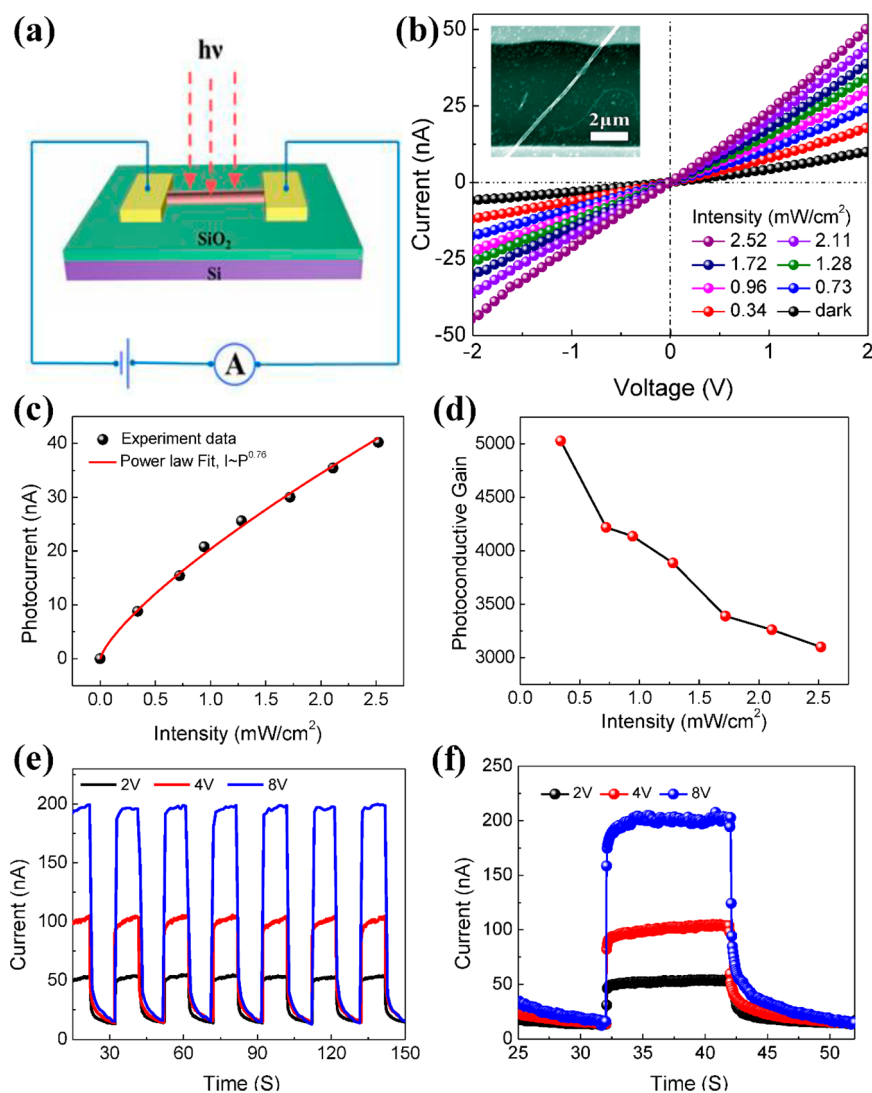
$$g_m = dI_{ds}/dV_{gs} \qquad (1)$$

Figure 2. Photoresponse properties of the single Cd₃P₂ NW photodetector on a rigid SiO₂/Si substrate. (a) Schematic illustration of a single NW photodetector. (b) $I-V$ curves of the device measured at room temperature in the dark and under illumination with green light (520 nm) of different intensities. The inset is a SEM image of the device. (c) Photocurrent *versus* light intensity plot at a bias of 2 V, with a power law dependence of $I \sim P^{0.76}$. (d) Photoconductive gain *versus* light intensity obtained at a bias of 2 V. (e) Photocurrent *versus* time plot of the single NW photodetector under illumination with green light (520 nm) at a bias of 2, 4, and 8 V. The light intensity was 2.52 mW/cm². (f) Photocurrent rise of the device at different bias voltages.

which is calculated to be 76.8 nA V^{-1}. The field-effect hole mobility μ_h thus can be calculated from the equation

$$\mu_h = g_m L^2/(V_{ds}C_i) \qquad (2)$$

where L (3.92 μm) is the NW length in the electrode channels and C_i is the capacitance of the back gate, which can be estimated from the equation

$$C_i \approx 2\pi\varepsilon_0\varepsilon_s L/\ln(2h/r) \qquad (3)$$

where h (500 nm) is the thickness of the dielectric SiO₂ layer, r (120 nm) is the NW radius, ε_0 is the vacuum dielectric constant ($\varepsilon_0 = 8.85 \times 10^{-12}$ F/m), and ε_s is the relative dielectric constant of SiO₂ ($\varepsilon_s = 3.9$). Eventually, the capacitance C_i and field-effect hole mobility μ_h can be calculated as 4.0×10^{-16} F and 2.94 cm² V^{-1} s^{-1}, respectively.

With a narrow direct band gap of 0.55 eV, the Cd₃P₂ NWs can in principle respond to ultraviolet, visible, and near-infrared light. In our work, photoresponses of the Cd₃P₂ NW FETs were characterized systematically. Figure 2a is the schematic illustration of a single Cd₃P₂ NW photodetector for photoresponse measurements under light illumination. A typical SEM image of the device is shown in the inset of Figure 2b. As shown, two Cr/Au (10 nm/100 nm) electrodes were deposited on both ends of the NWs, and the uncovered part of the NW was exposed to the irradiated light. The diameter of the Cd₃P₂ NWs and gap between two adjacent electrodes were about 240 nm and 8 μm, respectively. A monochromatic light was vertically shone on the device, and the corresponding photoresponse characteristics was recorded. The current–voltage ($I-V$) curves of the device have been measured

in the dark and under illumination with 520 nm light at different power intensities from 0.34 to 2.52 mW/cm^2, as shown in Figure 2b. It can be observed that, at the same voltage, the light current increases gradually with the increased light intensities. A high current of ~51.6 nA was recorded at an applied voltage of 2 V when the device was illuminated with 520 nm visible light at a power intensity of 2.52 mW/cm^2, while the dark current was only ~11.9 nA, the light current demonstrating the ultimately high sensitivity of the individual Cd$_3$P$_2$ NW photodetector.

Figure 2c depicts the dependence of the photocurrent on light intensities at a bias voltage of 2 V. Note that here the photocurrent is defined as the increment of the current caused by light illumination, namely, the difference between light current and dark current. The relationship can be fitted by the power law $I \sim P^{0.76}$, where I is the photocurrent and P is the incident light power intensity. Meanwhile, the photoconductive gain, which is defined as the number of charges collected by electrodes due to excitation by one photon, is also a key factor to reflect the sensitivity of photodetectors, and it can be expressed as $G = (I/P)(h\nu/e)$,[37] where ν is the frequency of the incident photon and e is the elemental electronic charge. The photoconductive gain versus light intensity of the Cd$_3$P$_2$ NW has been obtained at a bias voltage of 2 V and is plotted in Figure 2d. It can be seen that the highest photoconductive gain is 5029 for an intensity of 0.34 mW/cm^2, while higher intensity light leads to lower gain. This interesting behavior can be explained as follows. In general, it is known that surface band bending and space charge region in a NW can lead to high photoconductive gain.[44] However, the number of photogenerated carriers is increased when the device is irradiated under monochromatic visible light with increased power intensity. This can lead to flattening of the band bending, a weakened electron−hole pair separation capability, and a lower photoconductive gain. In addition, at high photon flux, carrier bimolecular recombination is also possible, which can contribute to shortening of carrier lifetime as well.[40,44] Nevertheless, the above result has shown that the Cd$_3$P$_2$ NW photodetector can achieve high sensitivity and performance for a low-intensity optical signal. This is a particularly attractive attribute for low-power optoelectronic applications. Figure 2e displays the photocurrent transient measurement by periodically turning on and off 520 nm light with a power intensity of 2.52 mW/cm^2 at different applied voltages (2, 4, and 8 V). It can be seen that at the identical light intensity the saturated photocurrent increases when the applied voltage is elevated. Meanwhile, under the same applied voltage, the photocurrent increases rapidly and reaches steady state at the "ON" state upon light illumination and then decreases quickly to the "OFF" state after the light is turned off, suggesting the
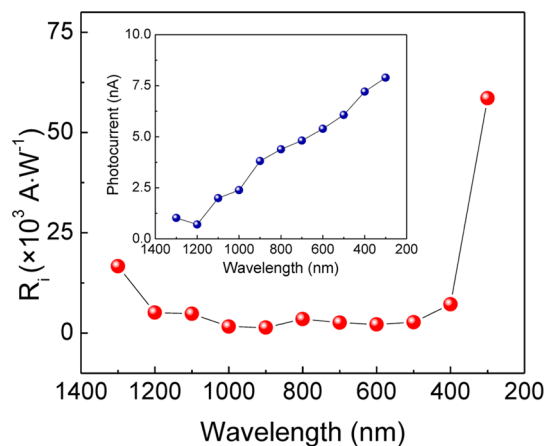

Figure 3. Spectral photoresponse of a single Cd$_3$P$_2$ NW device at different wavelengths from 300 to 1300 nm. The inset is the wavelength dependence of the photocurrent measured at a bias of 5 V.

excellent stability and reproducibility of the device. Specifically, the rise time at various applied voltages is shown in Figure 2f and estimated to be 0.1, 0.09, and 0.11 s, respectively. Furthermore, the responsivity (R_λ) of the device has been calculated. As one of the important figures-of-merit of a photodetector, R_λ can be defined as $R_\lambda = I/PS$,[38,39] where I is the photocurrent, P is the incident light intensity, and S is the NW effective illuminated area. For the single Cd$_3$P$_2$ NW device shown in Figure 2, $I = 40.2$ nA under 2 V bias, and $S = 1.23\ \mu m^2$. Based on these values, the R_λ of the photodetector irradiated by 520 nm light at 2.52 mW/cm^2 is 1296.9 A/W at a bias voltage of 2 V. Furthermore, the spectral photoresponse of the single Cd$_3$P$_2$ NW device has been achieved, as shown in the inset of Figure 3 (and Figure S2a), which covers the wavelength range from 300 to 1300 nm. As a result, the responsivity spectrum has been obtained, as shown in Figure 3. It clearly shows that the responsivity of this device ranges from 1.4×10^3 to 5.9×10^4 A·W^{-1} with the aforementioned wavelength range, showing a broadband photodetection characteristic. Note that the responsivity spectrum differs from the photocurrent spectrum, due to the wavelength-dependent intensity of the incident light, as shown in Figure S2b. It is known that noise equivalent power (NEP) is also one of the key figures-of-merit of a photodetector, which actually reflects the lowest optical power that a photodetector can respond to when the signal-to-noise ratio is 1. Typically, NEP $= (I_n^{21/2}/R_i)$(W),[53] where $I_n^{21/2}$ is the noise current root-mean-square (RMS) and R is the responsivity. According to the time-domain photocurrent measurement shown Figure S3 for 500 nm wavelength, the calculated RMS noise current is around 339 pA. Meanwhile, responsivity can be obtained from Figure 3 as 2682 A/W. Therefore, the NEP of the device for 500 nm wavelength can be estimated as 1.3×10^{-13} W (~0.13 pW). However, in practice, NEP is measured with the bandwidth (BW) of a photodetecor,
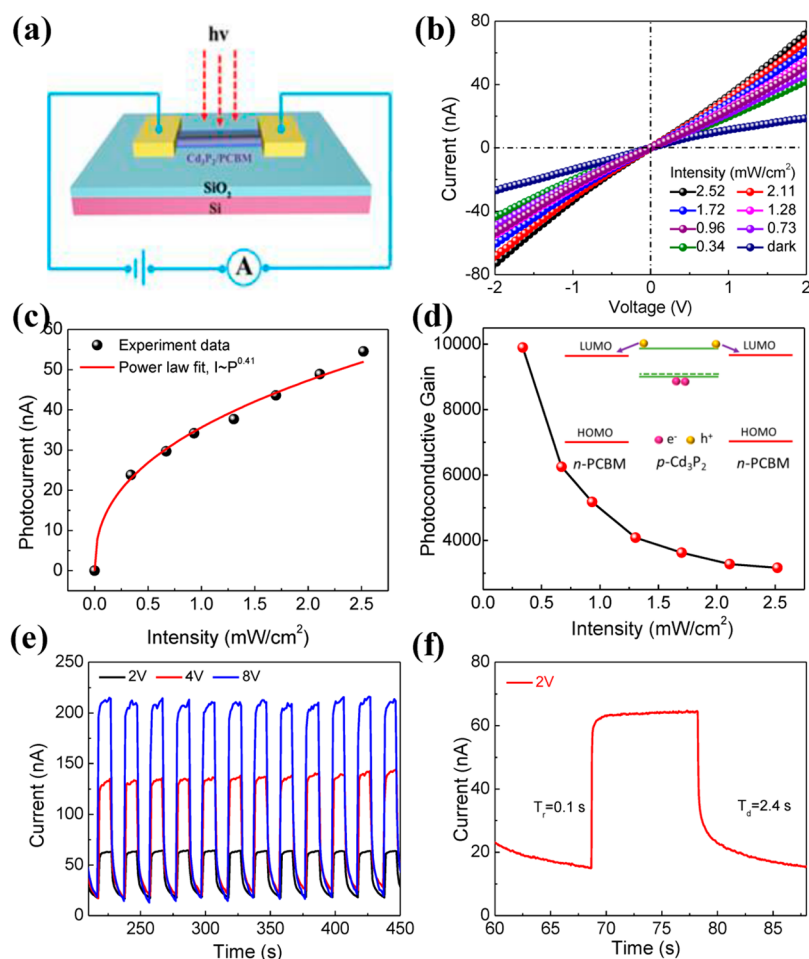
Figure 4. Photoresponse of a PCBM:Cd$_3$P$_2$ NW hybrid photodetector on a rigid SiO$_2$/Si substrate. The hybrid device was characterized at the same condition that was used for a pristine Cd$_3$P$_2$ NW photodetector. (a) Schematic illustration of the hybrid photodetector. (b) $I-V$ curves of the hybrid photodetector measured at room temperature in the dark and under illumination with green light (520 nm) of different intensities. (c) Photocurrent *versus* light intensity plot at a bias of 2 V. The corresponding function is $I \sim P^{0.41}$. (d) Photoconductive gain *versus* light intensity plot at a bias of 2 V. Inset shows the band diagram of this hybrid photodetector. (e) Photocurrent *versus* time plot of the device under illumination with green light (520 nm) at a bias of 2, 4, and 8 V. (f) Single light on/off cycle transient response of the device at a bias of 2 V with a light intensity of 2.52 mW/cm^2.

namely, NEP* = NEP × (BW)$^{-1/2}$.[56] Since the BW of a photodetector can be calculated from the transient response, BW = 2.2/(2$\pi\tau_d$), where τ_d = 3.2 s from Figure 2f is the decay time.[56] Therefore, BW = 0.11 Hz and NEP*$_{520nm}$ = 3.9 × 10^{-13} W/(Hz)$^{1/2}$ or 0.39 pW/(Hz)$^{1/2}$, which is comparable to the commercial Si photodetector (Newport, model 918D-UV-OD3R) with an NEP of 0.45 pW/(Hz)$^{1/2}$. However, photodetectors made of wide band gap materials, such as GaAs (Newport, model 818-BB-45), InP,[54] and GaN,[55] can have NEPs as low as 0.02−0.06 pW/(Hz)$^{1/2}$, due to much lower band-to-band noise.[56]

PCBM:Cd$_3$P$_2$ NW Photodetectors on a Rigid Silicon Substrate. Recently, organic−inorganic hybrid photodetectors have drawn considerable attention due to the fact that they can combine the merits of an organic semiconductor, such as large-scale production process, with low cost, easily tunable functionality, and exceptional mechanical flexibility, and those of the inorganic material, including superior intrinsic carrier mobility and broad-spectrum absorption capability. Therefore, hybridizing organic and inorganic materials may lead to high-performance devices with versatile functions and excellent flexibility.[41] In our work, in order to fabricate the hybrid organic/inorganic device, the Cd$_3$P$_2$ NWs in the same photodetector shown in Figure 2 were directly coated with a layer of PCBM. The schematic illustration of the hybrid device is shown in Figure 4a. Figure 4b shows the $I-V$ characteristics of this hybrid photodetector under irradiation of various power intensities. It can be conspicuously seen that the device current increases gradually as the light intensity increases. Figure 4c is the photocurrent *versus* light intensity plotted at a bias voltage of 2 V, and the corresponding power law fitting is $I \sim P^{0.41}$. Meanwhile, the photoconductive gain *versus* light intensity in Figure 4d was measured at a bias of 2 V. Similar to Figure 2d, the photoconductive gain decreases as the
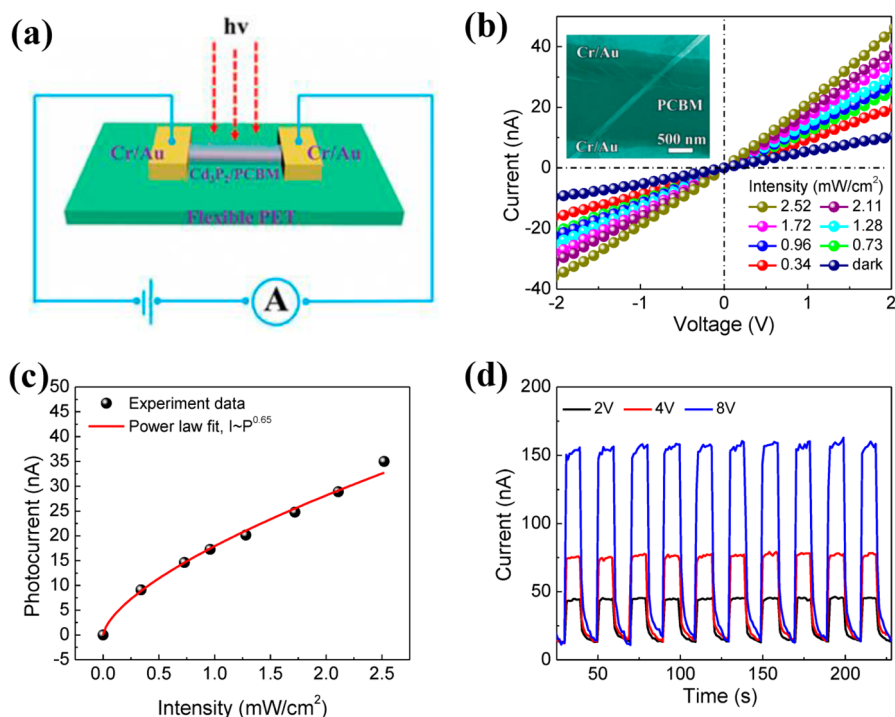
Figure 5. Photoresponse of PCBM:Cd3P2 NW photodetectors on a flexible PET substrate. (a) Schematic illustration of the hybrid photodetector. (b) $I-V$ **curves of the hybrid device in the dark and under 520 nm light irradiation with various power intensities. Inset shows the SEM image of the device. (c) Photocurrent** *versus* **light intensity curves of the device at an excitation wavelength of 520 nm and bias voltage of 2 V. The solid line shows a fitting of the power law** $I \sim P^{0.65}$ **. (d) Single on/off cycle transient response of the device under illumination with green light (520 nm) at a bias of 2, 4, and 8 V, respectively. The light power intensity was 2.52 mW/cm^2 for the above measurements.**

light intensity increases due to the same reason stated before. It is worth noting that at the light intensity of 0.34 mW/cm^2 the photoconductive gain of the hybrid device is close to 10 000, which is about twice that of the pristine Cd$_3$P$_2$ NW photodetector (R_{iCd3P2} = 5029). This fact clearly shows the advantage of the hybrid Cd$_3$P$_2$/PCBM structure. The time domain measurement of the hybrid photodetector was also conducted by periodically turning a 520 nm light on and off at different applied voltage (2, 4, and 8 V), as shown in Figure 4e. Compared with the pure Cd$_3$P$_2$ NW photodetector on the SiO$_2$/Si substrate (shown in Figure 2), the hybrid device has both higher dark current and photocurrent. The higher dark current may originate from the lower contact resistance, which is caused by the larger contact area of the hybrid device with the electrodes.[43] Meanwhile, it was also found that PCBM made a marginal contribution to the dark current, which will be further discussed later. Figure 4f shows the more detailed transient photocurrent of this hybrid device, which shows that the rise and decay time are around 0.1 and 2.4 s, respectively.

The above results indicate that the hybrid device on a rigid SiO$_2$/Si substrate has an excellent stability, reproducibility, and fast detection time. More importantly, it shows much improved photocurrent and photoconductive gain. This fact can be rationalized as follows. It is known that, due to the high surface-to-volume

ratio of NWs, surface trapping would drastically influence the carrier transport and photoconduction properties. For a p-type NW device, upon illumination with a photon energy above the band gap of Cd$_3$P$_2$, electron–hole pairs are generated and electrons can be readily trapped at the NW surface, leaving unpaired holes behind. This process not only results in an increase of the hole concentration and the increase of the photoconductivity but also suppresses electron–hole pair recombination due to the spatial separation of them.[44] Particularly for the PCBM:Cd$_3$P$_2$ hybrid device, due to the fact that Cd$_3$P$_2$ has a relatively low electron affinity of 4.0 eV,[51] while PCBM has a LUMO level at around 4.3 eV,[52] the possible band alignment can be schematically plotted as the inset of Figure 4d. In this scenario, the photoexcited electrons can be readily transferred to PCBM, leaving holes in the Cd$_3$P$_2$ nanowire for photoconduction. This unique configuration further improves the efficiency of spatial separation of electron–hole pairs, leading to a higher photocurrent and prolonged photocarrier lifetime. In fact, long photocarrier lifetime has been identified as the origin of high photoconductive gain previously.[44] This can also explain the higher photoconductive gain of the hybrid PCBM:Cd$_3$P$_2$ nanowire photodetector than that of the pristine Cd$_3$P$_2$ nanowire photodetector. On the other hand, as the photoconductivity of pure PCBM may affect the device performance, photoresponse

characteristics of the device made from pure PCBM are also studied and shown in Figure S4 in the Supporting Information. Notably, the dark current (about 0.5 nA) in the pure PCBM device at an applied voltage of 2 V is much lower than that of a single Cd_3P_2 NW (about 11.9 nA) and hybrid device (about 14 nA) at the same condition. The result is in agreement with a previous hybrid device based on a P_3HT:PCBM blend.[46] Meanwhile, for the pristine PCBM device, the photocurrent of 520 nm light illumination was relatively low and about 3.9 nA, which is much lower than the photocurrent of a single NW device (51.6 nA, shown in Figure 3e) and the hybrid device (65.5 nA, shown in Figure 4e). This can be explained by much lower carrier mobility in PCBM (0.21 cm^2/(V s)) as compared with that in Cd_3P_2 NWs. These results imply that the performance enhancement of the hybrid device is primarily contributed by formation of the junction interface and the favorable alignment of the conduction band to prolong the carrier lifetime.

Flexible PCBM:Cd_3P_2 NW Photodetectors. Due to the fast development of portable and flexible electronics, flexible sensors and detectors are in urgent need. In this work, flexible PCBM:Cd_3P_2 NW hybrid devices have been fabricated on a PET plastic substrate. The schematic illustration of a PCBM:single Cd_3P_2 NW hybrid device is shown in Figure 5a. The Cr/Au (10 nm/100 nm) electrodes are deposited on an individual NW dispersed on a flexible PET substrate. Figure 5b plots the I−V curves of the hybrid device measured in dark and under illumination with a green light (520 nm) with various different intensities, respectively. It can be observed from Figure 5c that the photocurrent increases gradually with light intensity when the same voltage of 2 V is applied, demonstrating a power law of $I \sim P^{0.65}$. As shown in Figure 5d, the flexible hybrid device exhibited reasonable sensitivity and stability to visible illumination with a current on/off ratio of 4.5, 7.6, and 15.3 for the applied voltage of 2, 4, and 8 V. The trend of these results is in agreement with that of the hybrid photodetector on a rigid SiO_2/Si substrate (Figure 4) and a pristine Cd_3P_2 NW photodetector on a flexible PET substrate (Figure S5).

In addition, it can be seen from Figure 5d that such a hybrid photodetector exhibited a dark current of 10.6 nA and photocurrent of 35 nA at 2 V bias. It is also found that, compared with the hybrid photodetector on a rigid substrate (shown in Figure 4e), the flexible hybrid photodetectors usually have a lower photocurrent, which may be related to the worse contact between the material and flexible PET substrate. However, as shown in Figure 5d and Figures S4 and S5, the photocurrent (35.5 nA) of the flexible hybrid device is usually higher than that of the pure Cd_3P_2 NW photodector (15.8 nA) on a flexible PET or pure PCBM device (3.5 nA), which also indicates the enhanced photoresponse characteristic of the flexible hybrid device. These results are also in accordance with the previous report of the
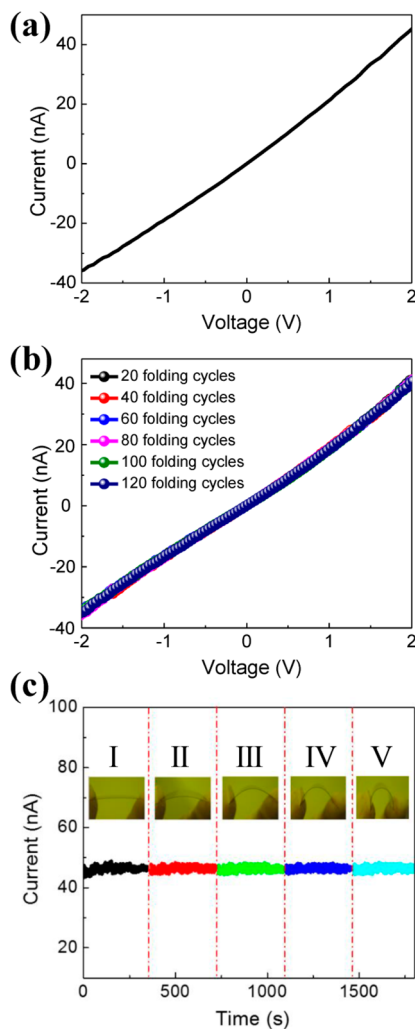

Figure 6. (a) I−V curves of the flexible hybrid devices under green light illumination before bending and (b) after 20, 40, 60, 80, 100, and 120 cycles of bending. (c) Current of the flexible hybrid photodetectors bent with various curvatures under a bias voltage of 2 V. The upper insets are the corresponding photographs of the device under five bending conditions.

hybrid organic−inorganic photodetectors.[42,45−50] To further study the broad-spectrum detection property of the organic−inorganic hybrid photodetectors and compare with that of the device fabricated on the rigid substrate, the photoresponse characteristics of both SiO_2/Si and PET devices were studied under three different wavelengths of light (980, 633, and 350 nm), which are in the range of NIR−visible−UV and shown in Figure S6a,c,e for the SiO_2/Si device and Figure S6b,d,f for the PET device. From these data, it can be clearly observed that both SiO_2/Si and flexible PET devices exhibit a fast, reversible, and stable photoresponse under the three wavelengths of light by periodically turning on or off the light illumination at a bias voltage of 2 V. The two kinds of hybrid photodetectors on SiO_2/Si and flexible PET substrates have a similar photoresponse, and both show a good sensitivity to a broad-spectrum range light.

In order to investigate the electrical stability of such a flexible hybrid photodetector, the photo-response of the device was also measured under different curvatures, as shown in Figure 6. In this measurement, the flexible hybrid device was first fixed onto two X−Y mechanical stages. By adjusting the distance between two adjacent stages, the bending curvatures of the device can be controlled. Figure 6a and b show the I−V curves of the flexible hybrid devices before and after bending for different cycles acquired with 520 nm wavelength illumination at 2.52 mW/cm^2 intensity. From the curves, it can be seen that, compared with the conductance of the flexible hybrid devices without bending (Figure 6a), the conductance of the device remained almost constant even after 20, 40, 60, 80, 100, and 120 cycles of bending, indicating the excellent folding toler-ance of the flexible PCBM:Cd$_3$P$_2$ NW hybrid device. In addition, the electrical current flow through the flexible hybrid device was marked at five different bending conditions, labeled as I, II, III, IV, and V in the upper insets in Figure 6c. It can be observed that the current nearly kept unchanged at a fixed voltage of 2 V, revealing the fact that the conductance of the device is hardly influenced by bending stress. This result demonstrates excellent mechanical flexibility

and electrical stability of the flexible PCBM:Cd$_3$P$_2$ hybrid device.

CONCLUSIONS

In conclusion, single-crystalline Cd$_3$P$_2$ NWs were synthesized via a CVD method to fabricate high-performance NW photodetectors with broad-spectrum response ranging from UV to infrared regions. It was discovered that the as-grown Cd$_3$P$_2$ NWs exhibited typical p-type semiconductor behavior with an elec-tron mobility of 2.94 cm^2 V^{-1} s^{-1} and a broad-spectrum detection ranging from UV−visible to NIR (300 to 1300 nm) with high photoconductive gain, responsiv-ity, stability, and reproducibility. Intriguingly, our in-vestigation has shown that by coating a layer of PCBM on the Cd$_3$P$_2$ NW device to form a hybrid organic/inorganic device configuration, device performance, especially photoconductive gain, can be largely im-proved, due to the more efficient photocarrier separation and prolonged carrier lifetime. Meanwhile, the hybrid photodetectors have also been fabricated on plastic substrates, demonstrating excellent flexibility and good electrical stability. These results have shown that p-type Cd$_3$P$_2$ NWs have a great potential for further applications in large-area, high-sensitivity, and high-speed photode-tection with a broad spectral photoresponse.

METHODS

Synthesis and Characterizations of Cd$_3$P$_2$ NWs. Cd$_3$P$_2$ NWs were prepared by a chemical vapor deposition process in a conven-tional horizontal furnace with a 25 mm inner diameter quartz tube. InP powder (99.999%, Aldrich) and Cd foil (length 4 cm × width 1 cm × thickness 0.1 cm, 99.99%) were used as the source. In a typical process, 0.3 g of InP powder was placed in the center heating zone of the furnace. A piece of precleaned Cd foil was then placed at the downstream position ∼15 cm away from the InP powders as the target substrate for NW growth. Prior to heating, the furnace was first pumped to clean the remaining air. Then, the system was rapidly heated to 900 °C with a rate of 30 °C/min and maintained at this temperature for 2 h. High-purity Ar at a constant flow rate of 100 sccm (standard cubic centimeters per minute) was admitted in as the protecting medium and carrier gas. After reaction, the furnace was cooled to room temperature naturally. Then a gray-black wool-like product was found deposited on the Cd foil. The as-synthesized product was collected for characterizations by field-emission scanning electron microscopy (Hitachi S4800) equipped with an energy-dispersive X-ray spectrometer and transmission elec-tron microscopy (JEOL JEM-3000F), respectively.

Fabrication of Single Cd$_3$P$_2$ NW Photodetectors and Hybrid PCBM:Cd$_3$P$_2$ Photodetectors on a Rigid and Flexible Substrate. The as-grown Cd$_3$P$_2$ NWs were removed by sonication from the Cd foil and subse-quently dispersed in 2-propanol, which was then dropped on a thermally oxidized Si substrate covered with a 500 nm SiO$_2$ layer and flexible PET substrate. The Cr/Au (10/100 nm) electrodes were patterned on top of the NWs using conventional photo-lithography, thermal evaporation, and a lift-off process. For the as-fabricated FETs, the underlying silicon substrate acted as the back gate. To prepare the hybrid device, PCBM (15 mg) was first dissolved in 1 mL of chloroform, and then the solution was dropped on the prepared Cd$_3$P$_2$ NW devices. For comparison, photodetectors based on pure PCBM film (0.1 mL) were also prepared via a similar process.

Electronic Transport and Photoresponse Measurements. The electric and photoresponse properties of the devices were measured using a four-probe station connected to a semiconductor characteriza-tion system (Keithley 4200-SCS). The spectroscopic responses were recorded by measuring a dc current at different wavelengths, from 300 to 1300, by using a xenon lamp (300 W). The incident power of the light was measured using an Ophir NOVA power meter. All measurements were performed in air and at room temperature.

Conflict of Interest: The authors declare no competing financial interest.

Supporting Information Available: EDS spectrum of the as-synthesized Cd$_3$P$_2$ nanowires is shown in Figure S1, photore-sponse characteristics of single Cd$_3$P$_2$ NW device under differ-ent wavelengths of light illumination at a bias voltage of 5 V are illustrated in Figure S2, photoresponse characteristics of a pure PCBM film photodetector are illustrated in Figure S4, photo-response properties of single Cd$_3$P$_2$ NW photodetectors on a flexible PET substrate are illustrated in Figure S5, and the reproducible on/off switching of PCBM:Cd$_3$P$_2$ NW hybrid photo-detectors on a rigid Si substrate and the flexible PET are illustrated in Figure S6. This material is available free of charge via the Internet at http://pubs.acs.org.

REFERENCES AND NOTES

1. Shen, G. Z.; Liang, B.; Wang, X. F.; Huang, H. T.; Chen, D.; Wang, Z. L. Ultrathin In$_2$O$_3$ NWs with Diameters below 4 nm: Synthesis, Reversible Wettability Switching Behavior, and Transparent Thin-Film Transistor Applications. *ACS Nano* **2011**, *5*, 6148–6155.

2. Shen, G. Z.; Liang, B.; Wang, X. F.; Chen, P. C.; Zhou, C. W. Indium Oxide Nanospirals Made of Kinked NWs. *ACS Nano* **2011**, *5*, 2155–2156.

3. Ju, S.; Facchetti, A.; Xuan, Y.; Liu, J.; Ishikawa, F.; Ye, P. D.; Zhou, C. W.; Marks, T. J.; Janes, D. B. Fabrication of Fully Transparent NW Transistors for Transparent and Flexible Electronics. *Nat. Nanotechnol.* **2007**, *2*, 378–384.

4. Wang, Z. X.; Safdar, M.; Jiang, C.; He, J. High-Performance UV-Visible-NIR Broad Spectral Photodetectors Based on One-Dimensional In$_2$Te$_3$ Nanostructures. *Nano Lett.* **2012**, *12*, 4715–4721.

5. Liu, Z.; Huang, H. T.; Liang, B.; Wang, X. F.; Wang, Z. R.; Chen, D.; Shen, G. Z. Zn$_2$GeO$_4$ and In$_2$Ge$_2$O$_7$ NW Mats Based Ultraviolet Photodetectors on Rigid and Flexible Substrates. *Opt. Express* **2012**, *20*, 2982–2991.

6. Fan, Z. Y.; Ho, J. C.; Jacobson, Z. A.; Yerushalmi, R.; Alley, R. L.; Razavi, H.; Javey, A. Wafer-Scale Assembly of Highly Ordered Semiconductor NW Arrays by Contact Printing. *Nano Lett.* **2008**, *8*, 20–25.

7. Liu, X.; Long, Y. Z.; Liao, L.; Duan, X. F.; Fan, Z. Y. Large-Scale Integration of Semiconductor NWs for High-Performance Flexible Electronics. *ACS Nano* **2012**, *6*, 1888–1900.

8. Liu, Z.; Chen, G.; Liang, B.; Yu, G.; Huang, H. T.; Chen, D.; Shen, G. Z. Fabrication of High-Quality ZnTe NWs toward High-Performance Rigid/Flexible Visible-Light Photodetectors. *Opt. Express* **2013**, *21*, 7799–7810.

9. Fan, Z. Y.; Chang, P. C.; Lu, J. G.; Walter, E. C.; Penner, R. M.; Lin, C. H.; Lee, H. P. Photoluminescence and Polarized Photodetection of Single ZnO NWs. *Appl. Phys. Lett.* **2004**, *85*, 6128–6130.

10. Fan, Z. Y.; Dutta, D.; Chien, C. J.; Chen, H. Y.; Brown, E. C.; Chang, P. C.; Liu, J. G. Electrical and Photoconductive Properties of Vertical ZnO NWs in High Density Arrays. *Appl. Phys. Lett.* **2006**, *89*, 213110–213110–3.

11. Wang, Z. R.; Wang, H.; Liu, B.; Qiu, W. Z.; Zhang, J.; Ran, S. H.; Huang, H. T.; Xu, J.; Han, H. W.; Chen, D.; *et al.* Transferable and Flexible Nanorod-Assembled TiO$_2$ Cloths for Dye-Sensitized Solar Cells, Photodetectors, and Photocatalysts. *ACS Nano* **2011**, *5*, 8412–8419.

12. Wang, Y. L.; Jiang, X. C.; Xia, Y. N. A Solution-Phase, Precursor Route to Polycrystalline SnO$_2$ NWs That Can Be Used for Gas Sensing under Ambient Conditions. *J. Am. Chem. Soc.* **2003**, *125*, 16176–16177.

13. Kuang, Q.; Lao, C. S.; Wang, Z. L.; Xie, Z. X.; Zheng, L. S. High-Sensitivity Humidity Sensor Based on a Single SnO$_2$ NW. *J. Am. Chem. Soc.* **2007**, *129*, 6070–6071.

14. Liu, B.; Zhang, J.; Wang, X. F.; Chen, G.; Chen, D.; Zhou, C. W.; Shen, G. Z. Hierarchical Three-Dimensional ZnCo$_2$O$_4$ NW Arrays/Carbon Cloth Anodes for a Novel Class of High-Performance Flexible Lithium-Ion Batteries. *Nano Lett.* **2012**, *12*, 3005–3011.

15. Ge, M. Y.; Rong, J. P.; Fang, X.; Zhou, C. W. Porous Doped Silicon NWs for Lithium Ion Battery Anode with Long Cycle Life. *Nano Lett.* **2012**, *12*, 2318–2323.

16. Park, C. M.; Sohn, H. J. Quasi-Intercalation and Facile Amorphization in Layered ZnSb for Li-Ion Batteries. *Adv. Mater.* **2010**, *22*, 47–52.

17. Fan, Z.; Razavi, H.; Do, J.-W.; Moriwaki, A.; Ergen, O.; Chueh, Y.-L.; Reichertz, L. A.; Brown, G. F.; Neale, S.; Yu, K.; *et al.* Three Dimensional Nanopillar Array Photovoltics on Low Cost and Flexible Substrates. *Nat. Mater.* **2009**, *8*, 648.

18. Tian, B. Z.; Zheng, X. L.; Kempa, T. J.; Fang, Y.; Yu, N. F.; Yu, G. H.; Huang, J. L.; Lieber, C. M. Coaxial Silicon NWs as Solar Cells and Nanoelectronic Power Sources. *Nature* **2007**, *449*, 885–888.

19. Chang, P.-C.; Fan, Z.; Tseng, W.-Y.; Rajagopal, A.; Lu, J. G. β-Ga2O3 NWs: Synthesis, Characterizations and p-Channel Field-Effect Transistor. *Appl. Phys. Lett.* **2005**, *87*, 222102.

20. Ford, A. C.; Ho, J. C.; Fan, Z.; Ergen, O.; Altoe, V.; Aloni, S.; Razavi, H.; Javey, A. Synthesis, Contact Printing, and Device Characterization of Ni-Catalyzed, Crystalline InAs NWs. *Nano Res.* **2008**, *1*, 32.

21. Skucha, K.; Fan, Z.; Jeon, K.; Javey, A.; Boser, B. Palladium/Silicon NW Schottky Barrier-Based Hydrogen Sensors. *Sensor Actuat. B: Chem.* **2010**, *145*, 232.

22. Zhang, F.; Ding, Y.; Zhang, Y.; Zhang, X. L.; Wang, Z. L. Piezo-phototronic Effect Enhanced Visible and Ultraviolet Photodetection Using a ZnO−CdS Core−Shell Micro/NW. *ACS Nano* **2012**, *7*, 9229–9236.

23. Liu, Z.; Luo, T.; Liang, B.; Chen, G.; Yu, G.; Xie, X. X.; Chen, D.; Shen, G. Z. High-Detectivity InAs NW Photodetectors with Spectral Response from Ultraviolet to Near-Infrared. *Nano Res.* **2013**, *6*, 775–783.

24. Hu, L. F.; Yan, J.; Liao, M. Y.; Xiang, H. J.; Gong, X. G.; Zhang, L. D.; Fang, X. S. An Optimized Ultraviolet-A Light Photodetector with Wide Range Photoresponse Based on ZnS/ZnO Biaxial Nanobelt. *Adv. Mater.* **2012**, *24*, 2305–2309.

25. Fan, Z. Y.; Ho, J. C.; Jacobson, Z. A.; Razavi, H.; Javey, A. Large-Scale, Heterogeneous Integration of NW Arrays for Image Sensor Circuitry. *Proc. Natl. Acad. Sci. U.S.A.* **2008**, *105*, 11066–11070.

26. Wang, J. J.; Cao, F. F.; Jiang, L.; Guo, Y. G.; Hu, W. P.; Wan, L. J. High Performance Photodetectors of Individual InSe Single Crystalline NW. *J. Am. Chem. Soc.* **2009**, *131*, 15602–15603.

27. Kind, H.; Yan, H. Q.; Messer, B.; Law, M.; Yan, P. D. NW Ultraviolet Photodetectors and Optical Switches. *Adv. Mater.* **2002**, *14*, 158–160.

28. Jie, J. S.; Zhang, W. J.; Jiang, Y.; Meng, X. M.; Li, Y. Q.; Lee, S. T. Photoconductive Characteristics of Single-Crystal CdS Nanoribbons. *Nano Lett.* **2006**, *6*, 1887–1892.

29. Shen, G. Z.; Chen, P. C.; Bando, Y.; Golberg, D.; Zhou, C. W. Bicrystalline Zn$_3$P$_2$ and Cd$_3$P$_2$ Nanobelts and Their Electronic Transport Properties. *Chem. Mater.* **2008**, *20*, 7319–7323.

30. Stepanchikov, D.; Shutov, S. Cadmium Phosphide as a New Material for Infrared Converters. *Semiconductor Phys., Quantum Electron Optoelectron.* **2006**, *9*, 40–44.

31. Shen, G. Z.; Bando, Y.; Ye, C. H.; Yuan, X. L.; Sekiguchi, T.; Golberg, D. Single-Crystal Nanotubes of II$_3$-V$_2$ Semiconductors. *Angew. Chem., Int. Ed.* **2006**, *118*, 7730–7734.

32. Green, M.; O'Brien, P. A Novel Synthesis of Cadmium Phosphide Nanoparticles Using the Single-Source Precursor [MeCdP^{t}Bu$_2$]$_3$. *Adv. Mater.* **1998**, *10*, 527–528.

33. Zhao, X. G.; Shi, J. L.; Hu, B.; Zhang, L. X.; Hua, Z. L. Confinement of Cd$_3$P$_2$ Nanoparticles Inside Ordered Pore Channels in Mesoporous Silica. *J. Mater. Chem.* **2003**, *13*, 399–403.

34. Shen, G. Z.; Bando, Y.; Golberg, D. Synthesis and Structures of High-Quality Single-Crystalline II$_3$-V$_2$ Semiconductors Nanobelts. *J. Phys. Chem. C* **2007**, *111*, 5044–5049.

35. Miao, S. D.; Hickey, S. G.; Rellinghaus, B.; Waurisch, C.; Eychmuller, A. Synthesis and Characterization of Cadmium Phosphide Quantum Dots Emittiong in the Visible Red to Near-Infrared. *J. Am. Chem. Soc.* **2010**, *132*, 5613–5615.

36. Wang, R. B.; Ratcliffe, C. I.; Wu, X. H.; Voznyy, O.; Tao, Y.; Yu, K. Magic-Sized Cd$_3$P$_2$ II-V Nanoparticles Exhibiting Bandgap Photoemission. *J. Phys. Chem. C* **2009**, *113*, 17979–17982.

37. Wu, P.; Dai, Y.; Ye, Y.; Yin, Y.; Dai, L. Fast-Speed and High-Gain Photodetectors of Individual Single Crystalline Zn$_3$P$_2$ NWs. *J. Mater. Chem.* **2011**, *21*, 2563–2567.

38. Li, L.; Wu, P. C.; Fang, X. S.; Zhai, T. Y.; Dai, L.; Liao, M. Y.; Koide, Y.; Wang, H. Q.; Bando, Y.; Golberg, D. Single-Crystalline CdS Nanobelts for Excellent Field-Emitters and Ultrahigh Quantum-Efficiency Photodetectors. *Adv. Mater.* **2010**, *22*, 3161–3165.

39. Yu, G.; Liang, B.; Huang, H. T.; Chen, G.; Liu, Z.; Chen, D.; Shen, G. S. Contact Printing of Horizontally-Aligned p-Type Zn$_3$P$_2$ NW Arrays for Rigid and Flexible Photodetectors. *Nanotechnology* **2013**, *24*, 095703.

40. Chen, M. W.; Chen, C. Y.; Lien, D.; Ding, Y.; He, J. H. Photoconductive Enhancement of Single ZnO NW

through Localized Schottky Effects. *Opt. Express* **2010**, *18*, 14836–14841.

41. Wang, X. F.; Song, W. F.; Liu, B.; Chen, G.; Chen, D.; Zhou, C. W.; Shen, G. Z. High-Performance Organic-Inorganic Hybrid Photodetectors Based on P$_3$HT:CdSe NWs Heterojunction on Rigid and Flexible Substrates. *Adv. Funct. Mater.* **2013**, *23*, 1202–1209.

42. Greenham, N. C.; Peng, X. G.; Alivisatos, A. P. Charge Separation and Transport in Conjugated-Polymer/ Semiconductor-Nanocrystal Composites Studied by Photoluminescence Quenching and Photoconductivity. *Phys. Rev. B* **1996**, *54*, 17628–17637.

43. Zhai, T. Y.; Fang, X. S.; Liao, M. Y.; Xu, X. J.; Li, L.; Liu, B. D.; Koide, Y.; Ma, Y.; Yao, J. N.; Bando, Y.; *et al.* Fabrication of High-Quality In$_2$Se$_3$ NW Arrays toward High-Performance Visible-Light Photodetectors. *ACS Nano* **2010**, *4*, 1596–1602.

44. Soci, C.; Zhang, A.; Xiang, B.; Dayeh, S. A.; Aplin, D. P. R.; Park, J.; Bao, X. Y.; Lo, Y. H.; Wang, D. ZnO NW UV Photodetectors with High Internal Gain. *Nano Lett.* **2007**, *7*, 1003–1009.

45. Huynh, W. U.; Dittmer, J. J.; Alivisatos, A. P. Hybrid Nanorod-Polymer Solar Cells. *Science* **2002**, *295*, 2425–2427.

46. Zhu, H. F.; Li, T.; Zhang, Y. J.; Dong, H. L.; Song, J. S.; Zhao, H. P.; Wei, Z. M.; Xu, W.; Hu, W. P.; Bo, Z. S. High-Performance Organic Nanoscale Photoswitches Based on Nanogap Electrodes Coated with a Blend of Poly-(3-hexylthiophene) and [6,6]-Phenyl-C61-butyric Acid Methyl Ester (P$_3$HT:PCBM). *Adv. Mater.* **2010**, *22*, 1645–1648.

47. Gunes, S.; Sariciftci, N. S. Hybrid Solar Cells. *Inorg. Chim. Acta* **2008**, *361*, 581–588.

48. Szendrei, K.; Cordella, F.; Kovalenko, M. V.; Boberl, M.; Hesser, G.; Yarema, M.; Jarzab, D.; Mikhnenko, O. V.; Gocalinska, A.; Saba, M.; *et al.* Solution-Processable Near-IR Photodetectors Based on Electron Transfer from PbS Nanocrystals to Fullerene Derivatives. *Adv. Mater.* **2009**, *21*, 683–687.

49. Wang, J. J.; Wang, Y. Q.; Cao, F. F.; Guo, Y. G.; Wan, L. J. Synthesis of Monodispersed Wurtzite Structure CuInSe$_2$ Nanocrystals and Their Application in High-Performance Organic−Inorganic Hybrid Photodetectors. *J. Am. Chem. Soc.* **2010**, *132*, 12218–12221.

50. Xue, D. J.; Wang, J. J; Wang, Y. Q.; Xin, S.; Guo, Y. G.; Wan, L. J. Facile Synthesis of Germanium Nanocrystals and Their Application in Organic-Inorganic Hybrid Photodetectors. *Adv. Mater.* **2011**, *23*, 3704–3707.

51. Freyland, W.; Goltzene, A.; Grosse, P.; Harbeke, G.; Lehmann, H.; Madelung, O.; Richter, W.; Schwab, C.; Madelung, C.; Weiser, G.; *et al. Physics of Non-Tetrahedrally Bonded Elements and Binary Compounds I*; Springer-Verlag: Berlin, 1983.

52. Scharber, M. C.; Mühlbacher, D.; Koppe, M.; Denk, P.; Waldauf, C.; Heeger, A. J.; Brabec, C. J. Design Rules for Donors in Bulk-Heterojunction Solar Cells—Towards 10% Energy-Conversion Efficiency. *Adv. Mater.* **2006**, *18*, 789–794.

53. Guo, F.; Yang, B.; Yuan, Y.; Xiao, Z.; Dong, Q.; Bi, Y.; Huang, J. A Nanocomposite Ultraviolet Photodetector Based on Interfacial Trap-Controlled Charge Injection. *Nat. Nanotechnol.* **2012**, *7*, 798–802.

54. Ho, W.; Liou, J.; Chen, C. Characterization of InP Based SAGCM Avalanche Photodetector for Single Photon Fiber Optic Communications. *PIERS Online* **2010**, *6*, 257–261.

55. Osinsky, A.; Gangopadhyay, S.; Gaska, R.; Williams, B.; Khan, M. A.; Kuksenkov, D.; Temkin, H. Low Noise p-π-n GaN Ultraviolet Photodetectors. *Appl. Phys. Lett.* **1997**, *71*, 2334–2336.

56. Decoster, D.; Harari, J. In *Optoelectronic Sensors*; Wiley-ISTE, 2010.